Electrochimica Acta 174 (2015) 78–86

Contents lists available at ScienceDirect

Electrochimica Acta

journal homepage: www.elsevier.com/locate/electacta

Electrochemical properties of carbon from oil palm kernel shell for high performance supercapacitors

Izan Izwan Misnon, Nurul Khairiyyah Mohd Zain, Radhiyah Abd Aziz, Baiju Vidyadharan, Rajan Jose *

Nanostructured Renewable Energy Materials Laboratory, Faculty of Industrial Science &Technology, Universiti Malaysia Pahang, Kuantan, 26300 Pahang, Malaysia

ARTICLE INFO

Article history:
Received 2 February 2015
Received in revised form 15 May 2015
Accepted 27 May 2015
Available online 30 May 2015

Keywords:
amorphous materials
supercapacitors
pseudocapacitors
energy storage

ABSTRACT

Electrochemical properties of activated carbon (AC) derived from oil palm kernel shell (PKS) are evaluated and compared with other biomass derived AC for fabricating high performance electrochemical double layer capacitors (EDLC). Cleaned PKS are carbonized by pyrolysis and subsequently activated by physical and chemical methods. The chemically AC show a wider pore distribution (1.4–9.3 nm) whereas the physically activated one has uniform pores (1.5 nm). The electrochemical properties of the two types of AC are evaluated using cyclic voltammetry (CV), charge–discharge cycling (CDC) and electrochemical impedance spectroscopy (EIS) in three-electrode configuration. High specific capacitance (C_S) (210 F g^{-1} in 1 M KOH electrolyte at 0.5 A g^{-1}) is obtained for chemically AC whereas the C_S for the physically AC is 50% lower (123 F g^{-1}). Galvanostatic CDC tests show that the electrodes maintained ~95–97% of C_S after 1000 cycles. The EIS revealed that the PKS AC has low series resistance (< 0.6 Ω) and relaxation time (~0.69 s) which would therefore offers high power density in the EDLC devices.

1. Introduction

Development of value-added commodities from waste bio-resources has two simultaneous impacts, viz. environmental remediation and wealth creation. Carbon, a functional material of high market value, is traditionally obtained from petroleum coke, pitch and coal; however, the non-renewability of these sources lead to search for alternatives such as biomass [1–3]. However, properties of carbon derived from biomass significantly vary; therefore, there is a dare need to optimize the source for a desired application. For electrochemical applications, a high specific surface area and pore volume would reduce the material need; and therefore, activated carbon (AC) with specific surface area as high as ~2000 $m^2 g^{-1}$ are routinely produced by chemical and physical methods [4,5]. The AC have attracted several industrial applications including electrodes for electrochemical double layer capacitor (EDLC) or also called supercapacitor, lithium ion batteries, hydrogen storage, catalyst host, adsorbents and healthcare [6–11]. For EDLC application, AC shows desirable performance in term of chemical stability, high electrical conductivity, and low cost. Although new generation allotropes of carbon such as carbon nanotubes and graphene offer higher electrical conductivity than the commercial AC, uniting their properties and mass production is a serious issue. The AC electrodes store electric charges via electrostatic charge accumulation at an electrode–electrolyte interface, which forms the basis of EDLC. Charging and discharging processes in the EDLC do not involve any chemical changes; therefore, these devices could be used for longer duration (10^4 – 10^6 cycles of charge–discharge) [12,13].

Currently, various AC from biomass precursors have been synthesized including utilization of coconut shell, wood, rice husk, walnut shell, banana peel, sugar cane bagasse, tea leaves and bamboo [9,10]. Chemical (ex: KOH, NaOH, $ZnCl_2$) and physical activation (ex: steam, CO_2) methods are routinely adopted for developing many biomass derived AC for EDLC application to enable specific capacitance (C_S) in the range 100–370 F g^{-1} in aqueous electrolytes [14–22]. Oil palm (*Elaeis Guineensis*), from whose fruits the palm oil is extracted, is fairly planted throughout the planet: a total of 15 million hectare of oil palm plantation is established, most of which is in the ASEAN region. The authors' country, Malaysia, alone offers ~5 million hectare of oil palm plantation. Over ~7.8 tons/hectare of processed fresh fruit bunches (FFB) are produced annually, 70% of which is removed as waste

* Corresponding author. Tel.: +6095492451; fax.: +6095492766
E-mail address: rjose@ump.edu.my (R. Jose).

http://dx.doi.org/10.1016/j.electacta.2015.05.163
0013-4686/

[23]. It is estimated that a total of ~100 million tons/year of biomass waste will be produced in the mill by the year 2020 in Malaysia alone, 8% of which is oil palm kernel shell (PKS) [23]. The PKS is a dry solid waste that yielded after palm oil extraction; the hardest portion that shows ease handling for carbon activation process. Due to the enormity of PKS, recycling them for value added products is highly desirable.

In this paper, to the best of our knowledge, we demonstrate the usefulness of AC from PKS for EDLC application for the first time. The PKS are relatively cheap (< USD 50/ton) and non-edible, thus ensure continuous material supply for industrial requirements. The PKS AC based EDLC electrodes gave C_S ~210 F g^{-1} for chemically activated samples, which is much higher than the value obtained for many biomass derived AC electrodes. Further electrochemical studies show that the PKS AC based electrodes have desirable charge–discharge cycling (CDC) stability, lower equivalent series resistance, and lower relaxation time to enable high power density in high energy density EDLC.

2. Experimental

2.1. Material preparation

The PKS was collected from processing mill, washed thoroughly with distilled water to remove soil and dirt and further dried at 100 °C in an oven. The dried PKS was then pyrolyzed at 500 °C in a furnace for 4 h. The as-obtained carbon powders were activated for improved specific surface area by chemical and physical activation methods; resulting samples are labeled as AC-C and AC-P, respectively. Aqueous potassium hydroxide (KOH, 6 M) was used as the chemical activating agent whereas physical activation was performed by means of steam. For chemical activation, the as-pyrolyzed carbon were mixed with KOH solution at a mass ratio of 1:4 and stirred for 4 h, dried at 100 °C in an oven and further heated in an electric furnace at 500 °C for 4 h. The annealed product was washed repeatedly with hydrochloric acid (HCl, 1 M) and then rinsed with distilled water until a neutral pH was obtained. For steam activation, the as-pyrolyzed carbon was placed inside the furnace, heated to 500 °C for 4 h in the presence of steam (25 cm^3/min) and subsequently dried at 100 °C in air. All pyrolysis and activation process is done under oxygen deficient environment.

2.2. Material Characterization

The AC was characterized by X-ray diffraction (XRD), Fourier transformed infrared spectroscopy (FTIR), gas adsorption studies, X-ray photoelectron spectroscopy (XPS) and field emission scanning electron microscopy (FESEM). The XRD patterns were acquired on Miniflex II (Rigaku, Japan) X-ray diffractometer employing CuKα radiation (λ = 1.5406 Å) and Ni- filter. Gas adsorption studies and Brunauer-Emmett-Teller (BET) specific surface area of the samples were obtained using ASAP 2020 (Micromeritics, USA) instrument. Functional groups of the sample were acquired on Spectrum One (Perkin Elmer, USA) FTIR spectrometer. Chemical analysis of the sample was obtained by XPS using Omicron NanoTechnology (ELS 5000, UK) X-ray photoelectron spectrometer. Surface morphology of the samples were investigated using a JSM-7800F (JEOL, Japan) FESEM.

2.3. EDLC Electrode Fabrication and Electrochemical Measurements

The electrodes for the electrochemical studies were prepared by mixing the dried AC (70 wt%.) with conducting carbon (Super P, 15 wt.%) and polyvinylidene fluoride (PVDF, 15 wt%)) binder using N-methylpyrrolidinone (NMP) as a solvent. The above mixture was stirred overnight and the slurry obtained thereby was coated onto a pre-cleaned nickel foam (pores per inch; 110ppi) substrate. The coated electrode was annealed at 60 °C in an oven for 24 h and finally pressed at 5 MPa using a hydraulic press. All electrodes were controlled to have ~1 cm^2 contact area with mass loading ~4 mg.

The electrochemical properties were evaluated by cyclic voltammetry (CV), galvanostatic CDC, and electrochemical impedance spectroscopy (EIS). The CV were obtained in the potential range of −1.0–0.0 V at various scan rates in three-electrode configuration using a potentiostat-galvanostat (Autolab PGSTAT 30, Eco Chemie B.V., The Netherlands). Galvanostatic CDC was obtained by cycling the potential from −1.0 to 0.0 V at different current densities in the range 10–0.5 A g^{-1}. Performance of the chemical and physically AC electrodes was compared in the 1 M KOH electrolyte. The a.c response of the EDLC electrode was studied by EIS in the frequency range 10 kHz to 10 mHz. All the electrochemical measurements were performed using the Autolab potentiostat using platinum as the counter electrode and Ag/AgCl as the reference electrode.

3. Results and discussion

3.1. X-Ray Diffraction Analysis

The XRD patterns of raw PKS, pyrolyzed PKS, AC-C and AC-P samples are in Fig. 1. The XRD pattern of the raw PKS (Fig. 1a) showed an intense and broad diffraction peak at 2θ = 24° (fwhm ~3.9°). This peak correspond to graphitic carbon structure of the biomass precursor [4,24], the intensity of which reduced and further broadened (fwhm ~5.9, 6.1, and 7.4° for pyrolyzed PKS, AC-C, and AC-P samples, respectively) upon carbonization and activation processes. The pyrolyzed and subsequently activated samples (Fig. 1b–d) show two major peaks centered at 2θ = 24 and 44° corresponds to (0 0 2) and (1 0 0) planes of carbon structure.

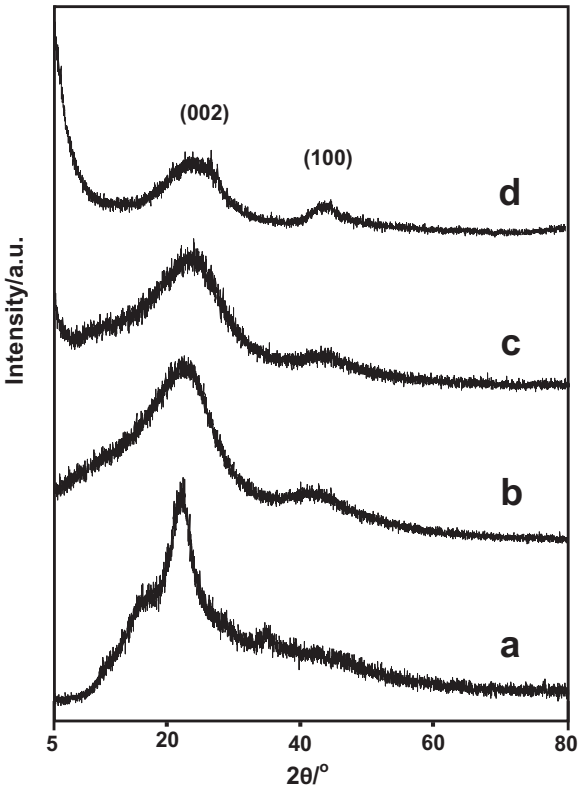

Fig. 1. XRD patterns of (a) raw PKS, (b) pyrolyzed PKS, (c) AC-C and (d) AC-P samples.

Broadening of the initial graphitic peak and appearance of new planes indicates that the PKS is further modified by the pyrolysis and activation processes. The broader peaks suggest that the carbon structure is amorphous and result from the destruction of initial graphitic structure during the pyrolysis and activation processes. The interlayer spacing (d_{002}) calculated using $2\theta = 24^\circ$ are 0.376 and 0.372 nm for AC-C and AC-P, respectively. Although the peaks present in the XRD patterns are rather broad, a study of the AC-C and AC-P structures can be tentatively approached to understand the structural details as previously reported [25–27]. The Debye–Scherrer Equation (Eq. (1)) [25] was used to estimates the mean crystallite dimension of the prepared AC and the results are tabulated in Table 1.

$$\left.\begin{aligned} L_c &= \frac{0.9\lambda}{\beta\cos\theta_{002}} \\ L_a &= \frac{1.94\lambda}{\beta\cos\theta_{100}} \end{aligned}\right\} \quad (1)$$

where L_c, L_a and β are average stacking height of crystallite, average staking weight of crystallite, and peak full width at half maximum, respectively.

All calculations are carried out by considering the instrumental error using silicon (Si) powder as reference. The activation methods result in different height and width of the crystallite staking. The L_c is higher for AC-C compared to AC-P, however the L_a is reversed. The ratio of L_c/L_a is a measure of edge orientation and corresponds to the relative density of the edge and basal plane of the crystallites [28]. The L_c/L_a of AC-C is 0.442 whereas that of AC-P is calculated to be 0.299. This deviation reflects the high edge plane fraction in AC-C whereas AC-P contains higher basal plane in the construction of the crystallites. Study by Pandolfo et al. observed that higher L_c/L_a ratio, as observed in AC-C, would lead to (i) increase of carbon conductivity and (ii) provide better ion diffusion to occur more rapidly at the edge of the crystallites and contribute to improved electrochemical performance [29]. Previous studies show that AC containing more edge planes are favorable in (i) increasing the C_S in electrochemical analysis, (ii) reducing the irreversible capacity loss and coulombic efficiency for AC electrodes and (iii) increasing the stronger bonding of surface functional groups [5,28,30]. Therefore, AC-C would be ideal for EDLC application. The mean number of layer planes (N_p) in the crystallite is higher in the AC-C and this feature is expected to contribute to better ion adsorption in each crystallite. The d, L_c, L_a and N_p values are comparable with other AC that prepared by utilizing nitrogen gas during heat treatment [25].

It should be pointed out that the peaks in the XRD pattern in Fig. 1 are rather broad; therefore, the calculated d, L_c, L_a and N_p values could be slightly over estimated. Nevertheless, the values determined using this procedure very well explain the electrochemical properties of the AC developed herewith, which will be discussed in section 3.6.

3.2. FTIR analysis

The functional groups on the surface of AC were studied using FTIR and the spectra are shown in Fig. 2. Both AC-C (Fig. 2a) and AC-P (Fig. 2b) showed almost similar pattern on the FTIR spectra. The broad and strong peaks at 3418 cm^{-1} for both AC corresponds to the -O–H stretching. These peaks would result from the physisorbed water molecule or hydroxyl groups on the AC surface. Two peaks at 2924 and 2848 cm^{-1} are the asymmetric and symmetric C-H stretching and the peak at 1386 cm^{-1} is the deformation mode of the C-H group [31]. A weak peak at 1748 cm^{-1} on AC-C is assigned to the stretching of C=O from and the one at 1580 cm^{-1} is attribute to the stretching mode of C=C, both originated from carbonyl group on the AC [32]. These two peaks are not clearly observed in the AC-P sample. Finally, the C–O–C stretching mode was observed at 1070 cm^{-1} [33]. From FTIR analysis, comparison of functional groups on different activation method can be verified and chemical activation produces an AC with various functional groups.

Table 1
Results of Debye – Scherrer analysis of the AC.

Carbon	d_{002} (nm)	d_{100} (nm)	L_c (nm)	L_a (nm)	L_c/L_a	N_p (L_c/d_{002})
AC-C	0.376	0.205	1.368	3.093	0.442	3.634
AC-P	0.372	0.210	1.116	3.740	0.299	3.000

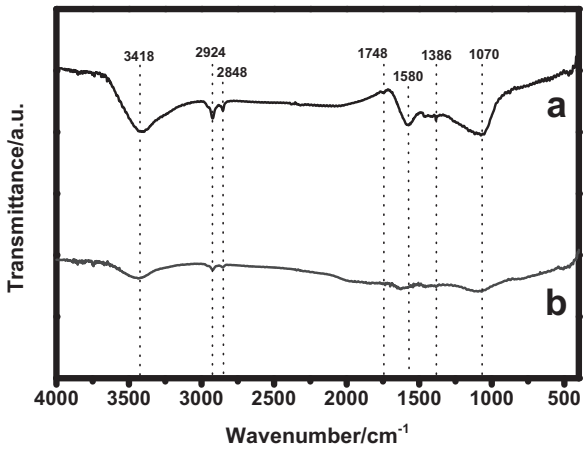

Fig. 2. FTIR spectra for (a) AC-C and (b) AC-P.

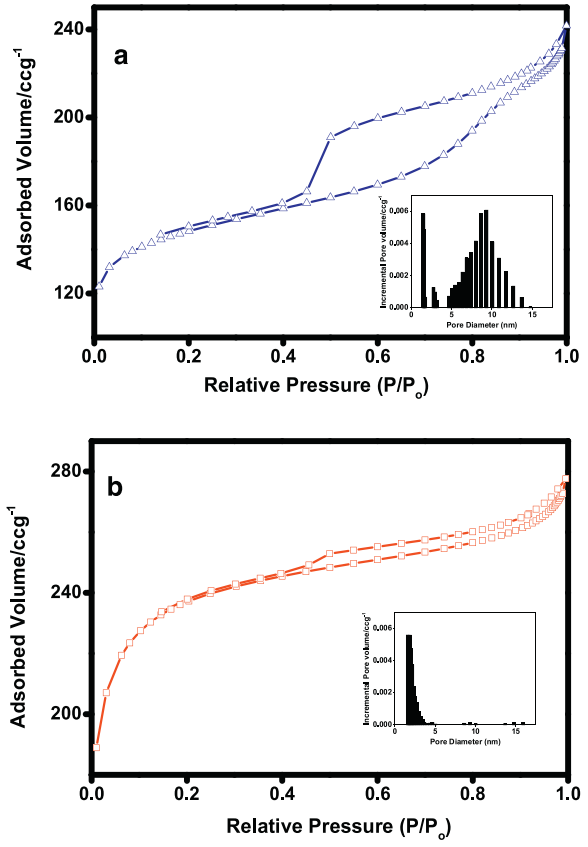

Fig. 3. Nitrogen adsorption/desorption isotherm for (a) AC-C and (b) AC-P samples. Insets are the pore size distribution for each AC.

3.3. Gas adsorption analysis

Fig. 3 shows the nitrogen adsorption–desorption isotherm for both AC at 77 K. The hysteresis loop for AC-C (Fig. 3a) corresponds to a combination of Type I and IV isotherms at $P/P_0 > 0.4$ indicating a combination of micropores and mesopores in the samples. The distribution of pore diameter (inset Fig. 3a) reveal micropores centered at 1.4 nm and the mesopores is centered at 9.3 nm. The AC-P hysteresis loop (Fig. 3b) belongs to Type I isotherm and mainly consist of micropores centered at 1.5 nm on the pore diameter distribution (inset Fig. 3b). Detailed surface and particulate properties of the AC are tabulated in the Table 2. The ratios of S_{micro}/S_{BET} are 0.66 and 0.71 whereas the ratios of V_{micro}/V_{total} are 0.45 and 0.65 for AC-C and AC-P, respectively. These quantities indicate that mesopore rich surface of the AC provides ion accessibility by channeling wider transport to micropore and the chemical activation on the PKS tend to produce AC enriched with mesopores structure [4].

3.4. XPS analysis

The XPS analysis for both ACs in full range of binding energy is shown in Fig. 4. The binding energy for carbon, nitrogen and oxygen are centered at 285, 405 and 532 eV respectively. The chemical composition of the AC determined from the XPS analysis is shown in Table 3. The carbon percentage in AC-C (Fig. 4a) and AC-P (Fig. 4b) are 80.22 and 64.21%, respectively. For both AC, oxygen and nitrogen are observed, most likely because the pyrolysis was undertaken in the ambient conditions. Presence of oxygen and nitrogen was also observed during carbonization in nitrogen atmosphere; nevertheless, these elements are beneficial on the surface functionalities of carbon by contributing the pseudocapacitance (PC) effect in charge storage mechanism [34–37].

3.5. FESEM analysis

The FESEM images of the surface morphologies of AC are depicted in Fig. 5. The AC synthesized using chemical and physical activation produce almost similar morphologies. The AC surface composed of pores with tunnel shape and honeycomb-like morphologies. Using Image J software, the calculated average holes diameter on its surface is ~1.6 μm. Creation of tunnels and holes during activation processes are beneficial for the ions adsorption and transport in charge storage mechanism.

3.6. Capacitive performance of chemical and physical activation of PKS

3.6.1. CV and Galvanostatic CDC cycling

The CV analysis was performed to probe the charge accumulation on the surface of the AC electrodes. Fig. 6a&b shows the CV curve of AC derived from PKS at different scan rate of 10 to 150 mV s^{-1} and potential range of -1.0 to 0.0 V. The CV curve of AC-C and AC-P showed similar quasi-rectangular shape at this scan rate region indicating EDLC behavior in charge storage mechanism. To clearly compare the charge accumulation of both AC surface, Fig. 6c depicts the CV behavior of AC-C and AC-P measured at

Table 2
Nitrogen adsorption–desorption data for the two AC. The S_{micro}, V_{micro}, and V_{total} are the specific surface area due to micropores, total volume of the micropores, and total pore volume of the samples, respectively; S_{BET} is the BET surface area.

Activated Carbon	AC-C	AC-P
S_{BET} ($m^2 g^{-1}$)	462.1	727.3
S_{micro} ($m^2 g^{-1}$)	304.6	513.1
V_{total}($cm^3 g^{-1}$)	0.354	0.420
V_{micro} ($cm^3 g^{-1}$)	0.161	0.273

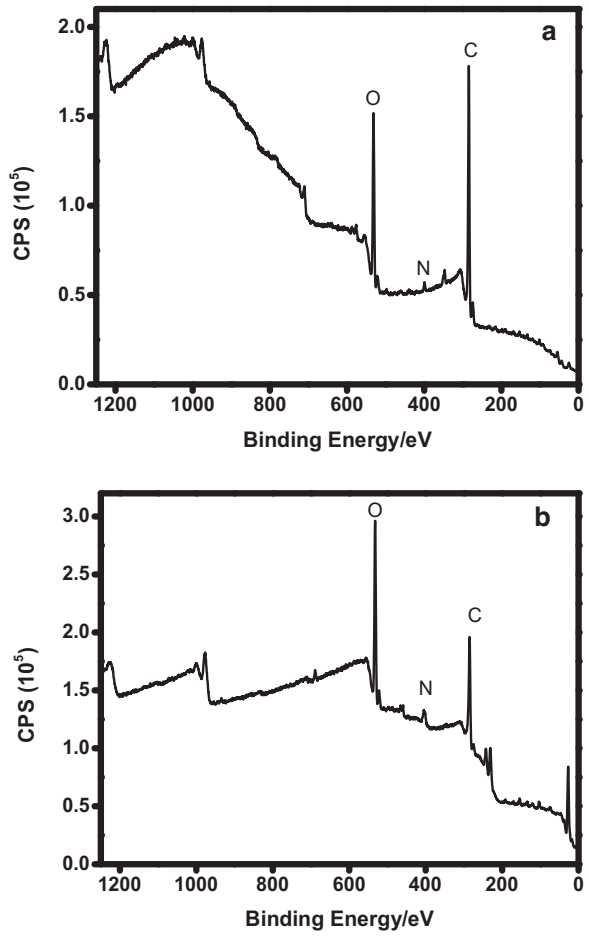

Fig. 4. XPS spectra of (a) AC-C and (b) AC-P samples.

Table 3
XPS characterization of AC.

Sample	XPS (at. %)		
	C	O	N
AC-C	80.22	18.51	1.26
AC-P	64.21	28.98	6.81

10 mV s^{-1}. Shapes of the CV curves are quasi-rectangular in both cases; however, AC-P showed a better rectangular shape than that of the AC-C. This observation indicates that EDLC mechanism alone operates in AC-P electrode as current is relatively stable with the increase in voltage. On the other hand, the current density of AC-C is nearly two-fold higher, which indicate that higher capacitance can be delivered by this material. The C_S of the electrodes was estimated from the cathodic part of the CV data using the equation,

$$C_S = \frac{\int i.dv}{vmV} \quad (2)$$

where i, v, m and V are current (A), scan rate (mV s^{-1}), mass-loading (g) and potential window (V), respectively. Variation of C_S as a function of scan rate is presented in Fig. 6d. No scan rate dependence in C_S was observed for the AC-P electrodes consistent with its CV showing near rectangular shape. On the other hand, the AC-C electrode showed a weak dependence of C_S on scan rate because the surface functional groups offer faradic reactions. The calculated C_S of the electrodes from the CV data at a scan rate of 10 mV s^{-1} for AC-C and AC-P are 211 and 112 F g^{-1}, respectively. The

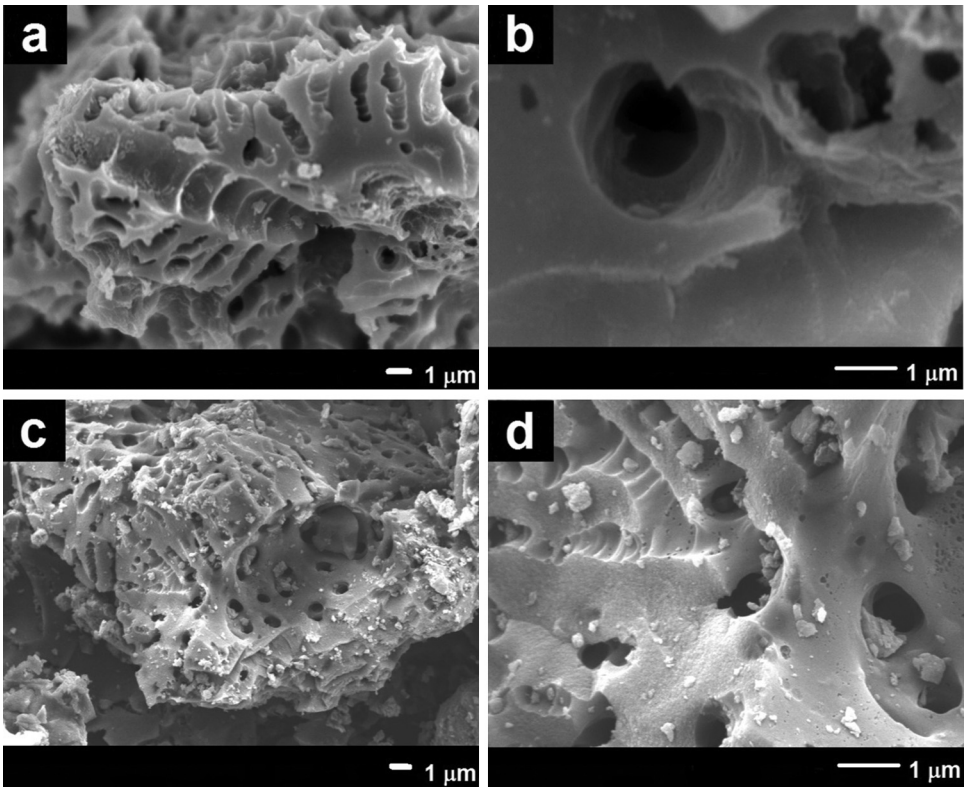

Fig. 5. FESEM micrograph for AC-C (a,b) and AC-P (c,d) at low and high magnifications.

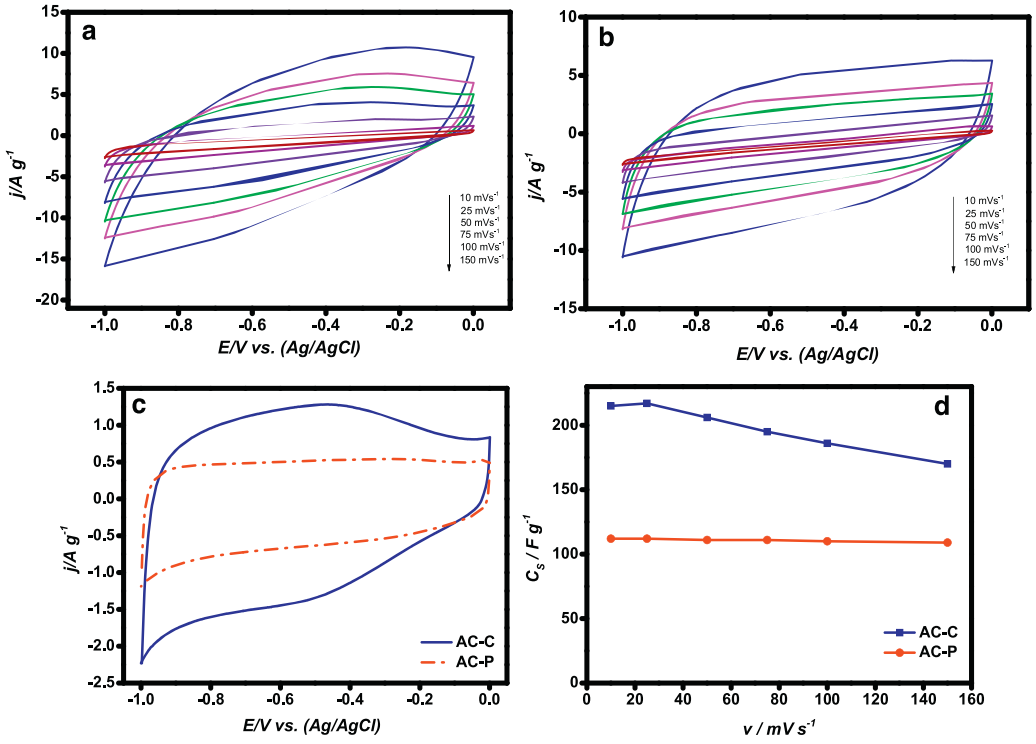

Fig. 6. CV curve of (a) AC-C and (b) AC-P in 1 M KOH at scan rate from 10 to 150 mV s^{-1}; (c) Comparison of CV curves for AC-C and AC-P at scan rate 10 mV s^{-1} and (d) dependence of C_S on the scan rate of CV.

enhanced C_S of AC-C originates from the combination of EDLC and PC reactions due to the presence of surface functional groups (C–O, C=O and COOH) developed during the chemical activation process [5].

Apart from surface functional groups that gave the EDLC and PC mechanism that operate in each electrode, porosity also play a dominant role in the generation of C_S values. Wu et al. observed that in chemical activation method, AC contains larger pores and

higher proportion of mesopores while physical activation generates AC with uniform ink-bottle type of pores [17]. The pores in AC-P (1.5 nm) hindered the dynamics of solvated electrolyte ion compared to AC-C (1.4 and 9.3 nm) and resulted in lower C_S. The reversibility of electrode materials for EDLC are usually evaluated by the dependency pattern of voltammetric currents to the scan rate of CV curve [17]. The analysis for AC-C and AC-P obtained at various potentials in 1 M KOH is shown in Fig. 7. The linear dependency of the voltammetric current with respect to scan rate indicates that charge and discharge currents are typically double layer capacitive. This linear dependency suggests high reversibility in electrochemical response for both electrodes, thereby fulfilling the basic requirements as an electrode material.

The CDC cycling behaviour of AC-C and AC-P was tested at current density in range of 0.5 to 10 A g^{-1} at potential window -1.0 V to 0.0 V. Fig. 8a&b shows the typical CDC behavior of AC-C and AC-P in 1 M KOH electrolyte. Fig. 8c compares CDC curves recorded at a current density of 1 A g^{-1} for the AC developed using the two processes. The CDC curves exhibit near triangular shape (Fig. 8c) indicates ideal charging and discharging behavior of the electrode. The small internal resistance (IR) drop at the beginning of the discharge process is associated with the series resistance (R_S); i.e., total resistance of the electrode. The AC-C electrode displayed longer charging and discharging time compared to the AC-P electrode, which is expected to arise from the functional groups on the AC-C surface leading to larger C_S. The C_S for CDC analysis is calculated by,

$$C_S = \frac{it}{mV} \quad (3)$$

where t is the discharge time required for each applied current. The variation of C_S for AC-C and AC-P determined from the CDC curves as a function of current density is shown in Fig. 8d. The C_S values are ranging from 80–210 F g^{-1} for AC-C and 41–123 F g^{-1} for AC-P when the current density varied between 10–0.5 A g^{-1}. This results compliment the CV analysis as depicted in Fig. 6d.

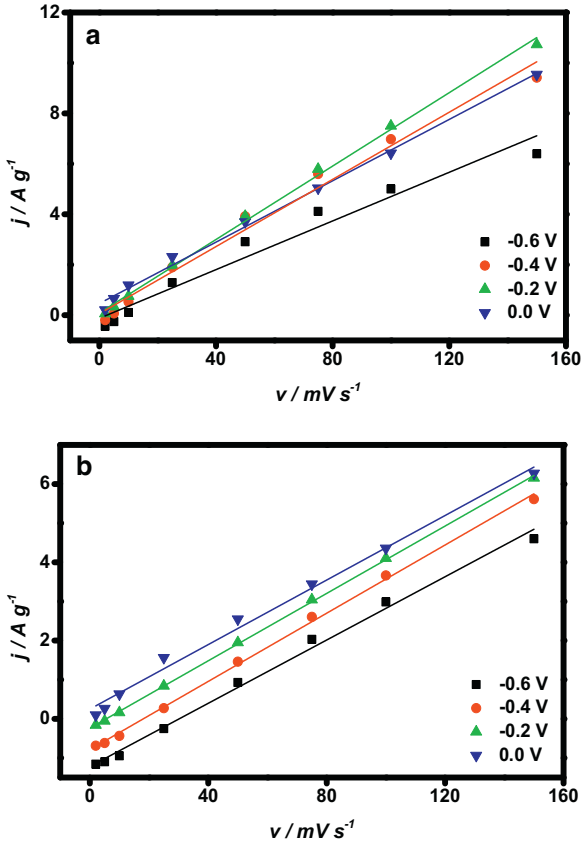

Fig. 7. Dependency pattern of volumetric current versus scan rate for (a) AC-C and (b) AC-P samples.

To conclude, both CV and CDC behavior in charge storage show larger charge accumulations in AC-C, which can be attributed to the following physical properties of AC (i) higher edge plane density, (ii) combination of micropores and mesopores structure widen the charge transport of ions, (iii) higher carbon crystallinity for charge transport and (iv) functional group that provide PC mechanism to occur on the AC surfaces.

To compare the performance of the PKS AC electrodes, a summary of performance of other biomass derived AC electrodes is presented in the Table 4. Properties of various electrodes are reported in different electrolytes as well as their specific surface areas strongly vary; therefore, a direct comparison is meaningless. The electrodes fabricated using AC from coffee bean waste, and argan leaves showed $C_S > 300$ F g^{-1} but in strong acid electrolytes. The tea leaves based electrode also showed $C_S > 300$ F g^{-1} in aqueous electrolytes but it has much larger surface than the other two. To compare the performance of previously reported AC, the areal capacitance (F cm^{-2}), which is defined as the normalized C_S respects to the specific surface area of the electrode material, has been calculated and shown in the Table 4 [38]. Although the PKS AC has lower surface areas compared to the others the AC-C electrode gave comparable C_S with the best performing electrodes such as those derived from tea leaves or coffee beans. The C_S of AC-C is superior to that produced from banana fiber, pistachio and coffee shells. This is in line with other finding that using seaweed as the biomass precursor that giving $S_{BET} \sim 400$ m^2 g^{-1} and found that the presence of high oxygen functional groups in the carbon surface enhance the C_S as high as 250 F g^{-1} [35,36].

The areal capacitance for AC-C is 45 μF cm^{-2} which is the highest among all the reported values for biomass based AC. Although waste coffee bean based electrodes show $C_S \sim 368$ F g^{-1} its areal capacitance is only 36 μF cm^{-2}. The areal capacitance for AC-P is lower compared to that of AC-C but still comparable with other AC electrodes. The larger areal capacitance observed for AC-C and AC-P suggest that most of the active surface contributed to the C_S. Moreover, C_S is a function of many parameters including pore distribution and its size, relationship between solvated ion size and pore size. The actively interacted surface of PKS AC with electrolyte through ion adsorption on the pores and subsequent charge accumulation on the electrode–electrolyte interface lead to higher C_S.

Finally to check the practical deployability of these electrodes, the electrochemical stability of the electrode under CDC cycling was tested using current density 5 A g^{-1} for 1000 cycle. As shown in Fig. 9, the capacitance retention from the initial C_S is 95 and 97% for AC-C and AC-P electrodes, respectively. There are initial capacitance drops in the first 50 cycles and the capacitance remains stable afterward. This indicates that AC prepared from PKS has good stability as EDLC electrode.

3.6.2. Electrochemical Impedance Spectroscopy Analyses

The EIS analysis was carried to further investigate the behaviour of AC-C and AC-P electrodes in range of 10 kHz – 10 mHz; Fig. 10a shows corresponding Nyquist plots. At the high frequency, the x–axis intercept corresponds to accumulation of contact resistance of the current collector–electrode and the ohmic resistance of the electrode–electrolyte interface, termed R_S [39]. The recorded R_S values are 0.56 and 0.6 Ω for AC-C and AC-P respectively. A semicircle is observed in the high to intermediate frequency region, the diameter of which corresponds to (i) passive layer on the nickel foam current collector and (ii) charge transfer resistance (R_{ct}) from the surface functionalities of AC surfaces and double

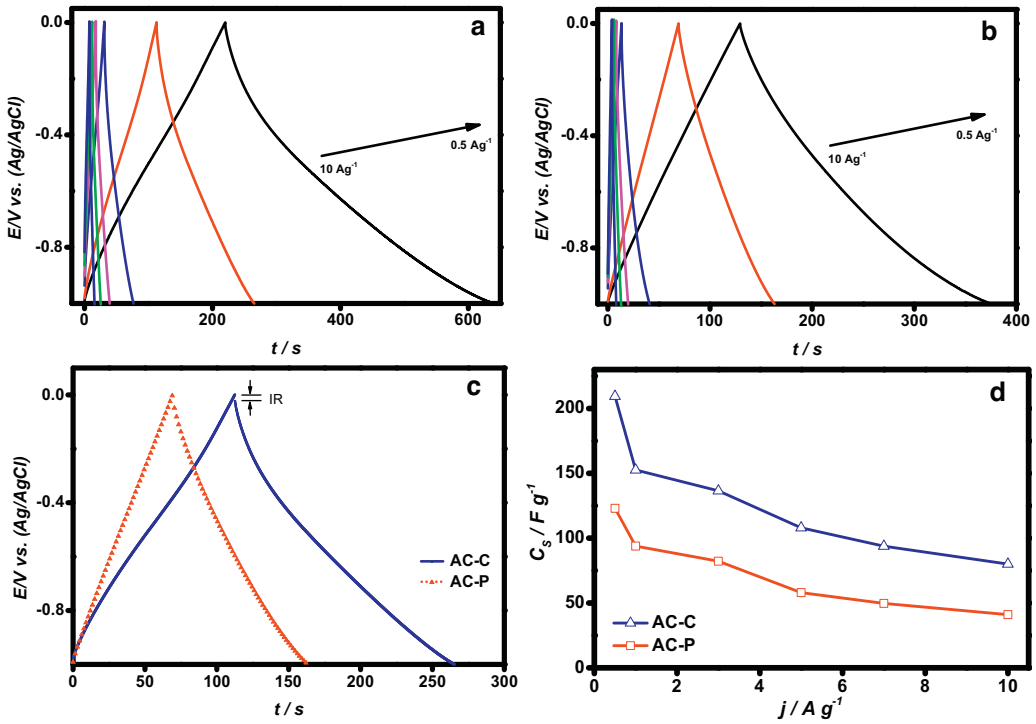

Fig. 8. The CDC behavior of (a) AC-C and (b) AC-P electrode in 1 M KOH electrolyte at potential window -1.0 to 0.0 V; (c) CDC curve for AC at 1 A g^{-1}; (d) C_S at various current densities.

Table 4
Comparison of AC derived from biomass precursor.

Biomass precursor	Activation Method	Pyrolisis Condition	S_{BET} ($m^2 g^{-1}$)	C_S ($F g^{-1}$)	Electrolyte	Areal Capacitance ($\mu F cm^{-2}$)	Ref.
Banana fiber	$ZnCl_2$	N_2	686	74	1M Na_2SO_4	11	[14]
Beer lees	KOH	N_2	3560	188	0.1 M H_2SO_4	3	[15]
Coffee Shell	$ZnCl_2$	N_2	842	156	6 M KOH	19	[16]
Pistachio shell	KOH	N_2	1009	125	HNO_3	12	[17]
Rice husk	NaOH	N_2	1886	210	3M KCl	11	[18]
Tea leaves	KOH	Ar	2841	330	2M KOH	12	[19]
Firwood	Steam	O_2 deficient	1130	142	1M HNO_3	13	[17]
Coffee bean	$ZnCl_2$	N_2	1019	368	1 M H_2SO_4	36	[20]
Argan seed shell	KOH/ melamine	N_2	2062	355	1 M H_2SO_4	17	[21]
Coconut shell	Steam	N_2	1532	228	6M KOH	15	[22]
Spinach leaves	KOH	N_2	2616	238	2M KOH	9	[50]
Ginkgo shell	KOH	N_2	1775	365	6M KOH	21	[51]
Oil Palm Kernel Shell	KOH	O_2 deficient	462.1	210	1M KOH	45	This work
Oil Palm Kernel Shell	Steam	O_2 deficient	727.3	123	1M KOH	17	This work

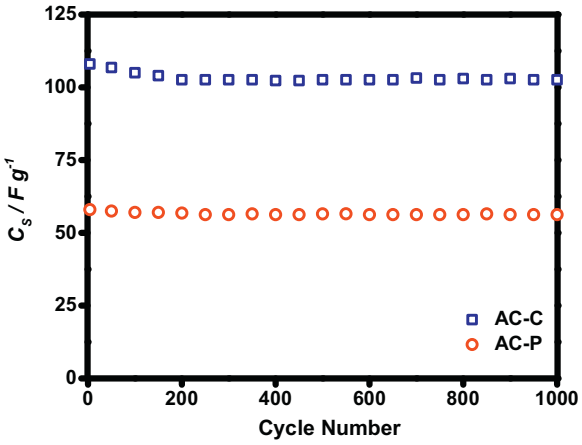

Fig. 9. Stability test of AC electrodes at current density 5 A g^{-1}.

layer capacitance (C_{dl}) [40–42]. It was observed that the semicircle diameter for AC-C is larger than AC-P (inset Fig. 10a), supporting the increasing C_S behavior as calculated from CV and CDC is related to the functional groups. In the low frequencies ranging from 5 Hz – 0.1 Hz, it showing the inclined portion of the curve (~45°) in the Nyquist plot. This behavior attributes to the distributed charge storage mechanism of the high surface area electrodes. The ions adsorption resistance into the porous network (micropores and mesopores) of carbon surface combines with increasing capacitive behavior [43]. A smaller segment indicates that capacitive behavior is dominant in pores whereas larger segment is corresponds to ion adsorption resistance is dominant in the mechanism. From the plot, AC-C is having slower ion adsorption; however, capacitive behavior is not dominant on the electrode. This behavior is due to dual pores characteristics (Fig. 3) of the material which increases the adsorption time. At the low frequency region, the straight line indicates the total capacitive behavior of charged electrode–electrolyte interface.

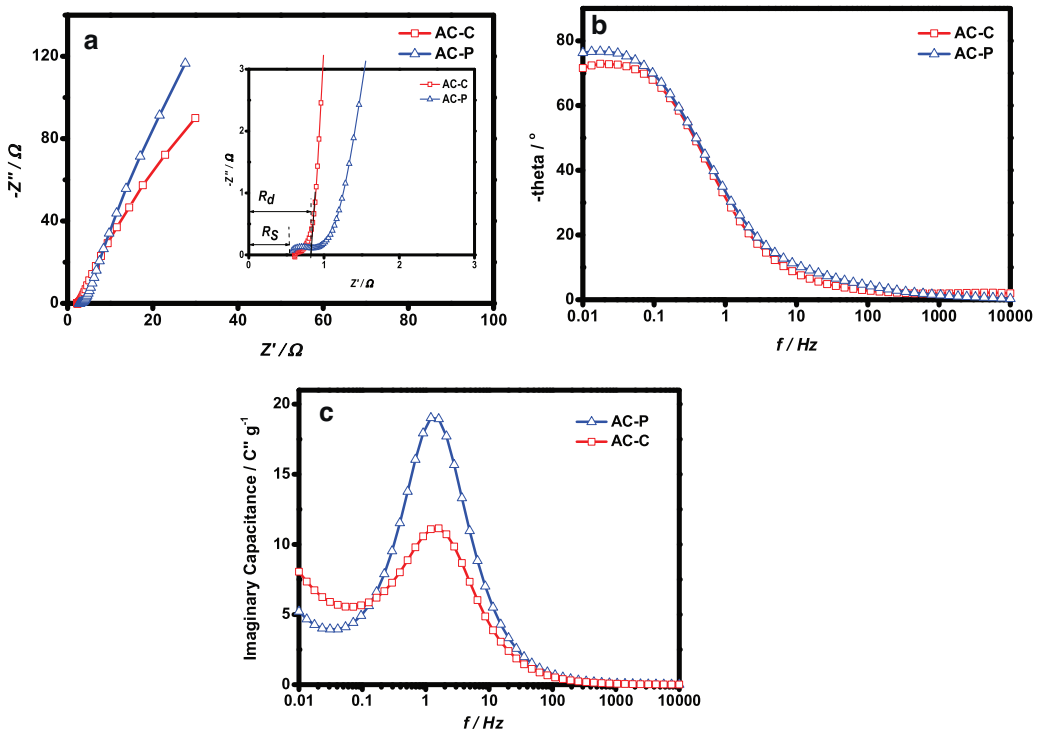

Fig. 10. (a) Nyquist plot of AC electrodes, Inset: a magnified portion at high frequency showing R_S and R_d; (b) Bode phase plot of AC electrodes; (c) Imaginary capacitance versus frequency of AC electrodes.

The equivalent distributed resistance (R_d) was obtained from the linear projection of the vertical region of Nyquist plot to the *x*-intercept on the real impedance and subtracting the R_S from the intersection (Inset of Fig. 10a) [43]. The R_d arises from the ions adsorption resistance into the porous (micropores and mesopores) network of carbon surface. Previous studies suggest that (i) material with higher micropores volume and (ii) poor pores conductivity network will lead to the decrease ion adsorption efficiency, thus increase the ions diffusion resistance [44–46]. The lower R_d value for AC-C is due to combination of mesopores and micropores structure on its surface that provides better pore accessibility to the electrolytes. The R_d values for AC-C and AC-P are 0.81 and 1.11 Ω respectively; therefore, another source of high C_S exhibited by AC-C is the observed low R_d.

Fig. 10b shows the Bode phase plot for both electrodes in 1 M KOH electrolyte. At high frequency, the low shift of the phase angle is controlled by the ionic resistance of the KOH electrolyte producing low capacitance value. However, at low frequency (< 10 Hz), both AC-C and AC-P electrode shows almost similar phase shift of ~ 80° indicates that the charge storage is primarily dominated by double layer mechanism [4,46]. This phase shift is different for PC type charge storage mechanism as shallower slope of the Bode plot will be observed.

To corroborate the supercapacitive performance of AC-C and AC-P, dielectric relaxation time constant (τ) or time required for the carbon to return to electrical neutrality after carrier injection or extraction processes is determined from the plot of the imaginary capacitance, C" using the relation [47];

$$C'' = \frac{-Z'(\omega)}{(\omega|Z(\omega)|^2 m)} \quad (4)$$

The C" showed a bell-shaped curve (Fig. 10c), the frequency corresponding to the peak (f_o) represents the point where the device changes from purely resistive to purely capacitive circuit and is a measure of τ defined by $\tau = {}^{1}/_{f_o}$. The τ value for both AC-C and AC-P is ~ 0.69 and 0.74 s respectively. This value provide indication to the power density (*P*) of material as $P = E/t$, where *E* and *t* are energy density and discharge time [48]. Lower value of τ is desirable as it will increase the value of *P*. The τ value for AC-P is 8% higher than AC-C, this might be result from the pores system of the material. The micropores density is bigger in AC-P (0.65) compare to AC-C (0.45) and this properties increase the discharge time mechanism of ions from the surface of AC [49].

4. Conclusion

In conclusion, we show that chemically activated carbon derived from palm kernel shells offer high areal capacitance (~45 μF cm^{-2}) when used as a supercapacitor electrode compared with corresponding steam activated (~17 μF cm^{-2}) as well as that developed from other biomass-derived carbon electrodes (≤ 36 μF cm^{-2}). The chemically activated carbon showed high specific capacitance of ~210 F g^{-1} in 1 M KOH electrolyte at 0.5 A g^{-1} whereas the performance of physically activated one was 50% lower (123 F g^{-1}). The electrodes maintained ~95–97 % of capacitance after 1000 cycles. The reason for this difference has been correlated from physico-chemical characterization of the two types of carbon derived from PKS. Chemically activated carbon shows both micropores and mesopores which facilitated channeling of ions movement (from mesopores to micropores) on the electrode surface and enhanced its electrochemical performance. On the other hand, physically activated carbon contains only micropores centered at 1.5 nm which limits the ions insertion/extraction process to be only at the carbon surface. The chemically activated carbon showed a high crystallinity than the physically activated carbon as shown by the higher edge density and mean number of layer planes. This provides higher electrical conductivity and resulted in enhanced C_S. Furthermore, the chemically activated carbon showed higher carbon content and functional groups. Origin of the higher capacitance in chemically activated carbon has been investigated using EIS measurements. The studies

showed that these electrodes have lower series resistance (0.56 Ω), equivalent distributed resistance (0.81 Ω), and relaxation time (0.69 s) than the electrodes prepared from physically activated carbon. Owing to the enormity PKS (over 100 tons/year in Malaysia alone), carbon could be produced in appreciable quantities from this source; therefore, the present results have would be useful to sustain an industry.

Acknowledgements

This work was supported by Malaysian Technical University Network (MTUN) Gallery Showcase Research Grant (RDU131201) and Postgraduate Research Scheme of UMP (GRS 130317).

References

[1] L. Wei, G. Yushin, Nanostructured activated carbons from natural precursors for electrical double layer capacitors, Nano Energy 1 (2012) 552.
[2] P. Kalyani, A. Anitha, Biomass carbon & its prospects in electrochemical energy systems, Int. J. Hydrogen Energy 38 (2013) 4034.
[3] R. Madhu, S. Palanisamy, S.M. Chen, S. Piraman, A low temperature synthesis of activated carbon from the bio waste for simultaneous electrochemical determination of hydroquinone and catechol, J. Electroanal. Chem. 727 (2014) 84.
[4] M. Biswal, A. Banerjee, M. Deo, S. Ogale, From dead leaves to high energy density supercapacitors, Energy Environ. Sci. 6 (2013) 1249.
[5] F. Wang, S. Xiao, Y. Hou, C. Hu, L. Liu, Y. Wu, Electrode materials for aqueous asymmetric supercapacitors, RSC Adv. 3 (2013) 13059.
[6] R.J. White, V. Budarin, R. Luque, J.H. Clark, D.J. Macquarrie, Tuneable porous carbonaceous materials from renewable resources, Chem. Soc. Rev. 38 (2009) 3401.
[7] M. Kang, Y.S. Bae, C.H. Lee, Effect of heat treatment of activated carbon supports on the loading and activity of Pt catalyst, Carbon 43 (2005) 1512.
[8] S.K. Bhatia, A.L. Myers, Optimum conditions for adsorptive storage, Langmuir 22 (2006) 1688.
[9] A.C. Dillon, M.J. Heben, Hydrogen storage using carbon adsorbents: past, present and future, Appl. Phys. A-Mater. 72 (2001) 133.
[10] S. Flandrois, B. Simon, Carbon materials for lithium-ion rechargeable batteries, Carbon 37 (1999) 165.
[11] M. Hartmann, A. Vinu, G. Chandrasekar, Adsorption of vitamin E on mesoporous carbon molecular sieves, Chem. Mater. 17 (2005) 829.
[12] B.E. Conway, Electrochemical Supercapacitors: Scientific Fundamentals and Technological Applications, Kluwer Academic Press/Plenum Publishers, New York, 1999.
[13] P. Simon, Y. Gogotsi, Materials for electrochemical capacitors, Nat. Mater. 7 (2008) 845.
[14] V. Subramanian, C. Luo, A.M. Stephan, K.S. Nahm, S. Thomas, B. Wei, Supercapacitors from activated carbon derived from banana fibers, J. Phys. Chem. C 111 (2007) 7527.
[15] S.G. Lee, K.H. Park, W.G. Shim, M.S. Balathanigaimani, H. Moon, Performance of electrochemical double layer capacitors using highly porous activated carbons prepared from beer lees, J. Ind. Eng. Chem. 17 (2011) 450.
[16] M.R. Jisha, Y.J. Hwang, J.S. Shin, K.S. Nahm, T. Prem Kumar, K. Karthikeyan, N. Dhanikaivelu, D. Kalpana, N.G. Renganathan, A.M. Stephan, Electrochemical characterization of supercapacitors based on carbons derived from coffee shells, Mater. Chem. Phys. 115 (2009) 33.
[17] F.C. Wu, R.L. Tseng, C.C. Hu, C.C. Wang, Effects of pore structure and electrolyte on the capacitive characteristics of steam- and KOH-activated carbons for supercapacitors, J. Power Sources. 144 (2005) 302.
[18] Y. Guo, J. Qi, Y. Jiang, S. Yang, Z. Wang, H. Xu, Performance of electrical double layer capacitors with porous carbons derived from rice husk, Mater. Chem. Phys. 80 (2003) 704.
[19] C. Peng, X. Yan, R. Wang, J. Lang, Y. Ou, Q. Xue, Promising activated carbons derived from waste tea-leaves and their application in high performance supercapacitors electrodes, Electrochim. Acta 87 (2013) 401.
[20] T.E. Rufford, D.H. Jurcakova, Z. Zhu, G.Q. Lu, Nanoporous carbon electrode from waste coffee beans for high performance supercapacitors, Electrochem. Commun. 10 (2008) 1594.
[21] A. Elmouwahidi, Z.Z. Benabithe, F.C. Marín, C.M. Castilla, Activated carbons from KOH-activation of argan (Argania spinosa) seed shells as supercapacitor electrodes, Bioresour. Technol. 111 (2012) 185.
[22] J. Mi, X.R. Wang, R.J. Fan, W.H. Qu, W.C. Li, Coconut-shell-based porous carbons with a tunable micro/mesopore ratio for high-performance supercapacitors, Energy Fuels 26 (2012) 5321.
[23] National Biomass Strategy 2020: New wealth creation for Malaysia's palm oil industry, Kuala Lumpur, 2011.
[24] C.C. Huang, Y.Z. Chen, Electrochemical performance of supercapacitors with KOH activated mesophase carbon microbead electrodes, J. Taiwan Inst. Chem. Eng. 44 (2013) 611.
[25] P.J.M. Carrott, J.M.V. Nabais, M.M.L. Ribeiro Carrott, J.A. Pajares, Preparation of activated carbon fibres from acrylic textile fibres, Carbon 39 (2001) 1543.
[26] R. Farma, M. Deraman, A. Awitdrus, I.A. Talib, E. Taer, N.H. Basri, J.G. Manjunatha, M.M. Ishak, B.N.M. Dollah, S.A. Hashmi, Preparation of highly porous binderless activated carbon electrodes from fibres of oil palm empty fruit bunches for application in supercapacitors, Bioresour. Technol. 132 (2013) 254.
[27] J.M.V. Nabais, C.E.C. Laginhas, P.J.M. Carrott, M.M.L.R. Carrott, Production of activated carbons from almond shell, Fuel Process. Technol. 92 (2011) 234.
[28] D. Qu, Studies of the activated carbons used in double-layer supercapacitors, J. Power Sources 109 (2002) 403.
[29] A.G. Pandolfo, A.F. Hollenkamp, Carbon properties and their role in supercapacitors, J. Power Sources 157 (2006) 11.
[30] K. Zaghib, G. Nadeau, K. Kinoshita, Influence of edge and basal plane sites on the electrochemical behavior of flake-like natural graphite for Li-ion batteries, J. Power Sources 97–98 (2001) 97.
[31] B. Grzyb, C. Hildenbrand, S.B. Fabry, D. Bégin, N. Job, A. Rigacci, P. Achard, Functionalisation and chemical characterisation of cellulose-derived carbon aerogels, Carbon 48 (2010) 2297.
[32] J. Zheng, Q. Zhao, Z. Ye, Preparation and characterization of activated carbon fiber (ACF) from cotton woven waste, Appl. Surf. Sci. 299 (2014) 86.
[33] X.L. Wu, T. Wen, H.L. Guo, S. Yang, X. Wang, A.W. Xu, Biomass-derived sponge-like carbonaceous hydrogels and aerogels for supercapacitors, ACS Nano 7 (2013) 3589.
[34] M.P. Bichat, E. Raymundo-Piñero, F. Béguin, High voltage supercapacitor built with seaweed carbons in neutral aqueous electrolyte, Carbon 48 (2010) 4351.
[35] E. Raymundo-Piñero, F. Leroux, F. Béguin, A high-performance carbon for supercapacitors obtained by carbonization of a seaweed biopolymer, Adv. Mater. 18 (2006) 1877.
[36] E. Raymundo-Piñero, M. Cadek, F. Béguin, Tuning carbon materials for supercapacitors by direct pyrolysis of seaweeds, Adv. Funct. Mater. 19 (2009) 1032.
[37] M. Zhou, F. Pu, Z. Wang, S. Guan, Nitrogen-doped porous carbons through KOH activation with superior performance in supercapacitors, Carbon 68 (2014) 185.
[38] K. Wang, H. Wu, Y. Meng, Y. Zhang, Z. Wei, Integrated energy storage and electrochromic function in one flexible device: an energy storage smart window, Energy Environ. Sci. 5 (2012) 8384.
[39] R.A. Aziz, I.I. Misnon, K.F. Chong, M.M. Yusoff, R. Jose, Layered sodium titanate nanostructures as a new electrode for high energy density supercapacitors, Electrochim. Acta 113 (2013) 141.
[40] Q. Wang, Q. Cao, X. Wang, B. Jing, H. Kuang, L. Zhou, A high-capacity carbon prepared from renewable chicken feather biopolymer for supercapacitors, J. Power Sources 225 (2013) 101.
[41] G. Zhao, N. Zhang, K. Sun, Porous MoO_3 films with ultra-short relaxation time used for supercapacitors, Mater. Res. Bull. 48 (2013) 1328.
[42] W. Li, D. Chen, Z. Li, Y. Shi, Y. Wan, G. Wang, Z. Jiang, D. Zhao, Nitrogen-containing carbon spheres with very large uniform mesopores: The superior electrode materials for EDLC in organic electrolyte, Carbon 45 (2007) 1757.
[43] R. Kötz, M. Carlen, Principles and applications of electrochemical capacitors, Electrochim. Acta 45 (2000) 2483.
[44] J. Gamby, P. Taberna, P. Simon, J. Fauvarque, M. Chesneau, Studies and characterisations of various activated carbons used for carbon/carbon supercapacitors, J. Power Sources 101 (2001) 109.
[45] D. Weingarth, D. Cericola, F.C.F. Mornaghini, T. Hucke, R. Kötz, Carbon additives for electrical double layer capacitor electrodes, J. Power Sources 266 (2014) 475.
[46] F. Lufrano, P. Staiti, M. Minutoli, Evaluation of nafion based double layer capacitors by electrochemical impedance spectroscopy, J. Power Sources 124 (2003) 314.
[47] C. Portet, P.L. Taberna, P. Simon, E. Flahaut, C. Laberty-Robert, High power density electrodes for carbon supercapacitor applications, Electrochim. Acta 50 (2005) 4174.
[48] A.E. Fischer, M.P. Saunders, K.A. Pettigrew, D.R. Rolison, J.W. Long, Electroless deposition of nanoscale MnO_2 on ultraporous carbon nanoarchitectures: Correlation of evolving pore-solid structure and electrochemical performance, J. Electrochem. Soc. 155 (2008) A246.
[49] E. Frackowiak, F. Béguin, Carbon materials for the electrochemical storage of energy in capacitors, Carbon 39 (2001) 937.
[50] Y. Ou, C. Peng, J. Lang, D. Zhu, X. Yan, Hierarchical porous activated carbon produced from spinach leaves as an electrode material for an electric double layer capacitor, New Carbon Mater. 29 (2014) 209.
[51] L. Jiang, J. Yan, L. Hao, R. Xue, G. Sun, B. Yi, High rate performance activated carbons prepared from ginkgo shells for electrochemical supercapacitors, Carbon 56 (2013) 146.